Chinese Chemical Letters 34 (2023) 107760

Contents lists available at ScienceDirect

Chinese Chemical Letters

journal homepage: www.elsevier.com/locate/cclet

Calcium-organic frameworks cathode for high-stable aqueous Zn/organic batteries

Wenshan Gou[a], Tian Jiang[b], Wei Wang[c], Qi Fan[b,*], Yan Zhang[a,*]

[a] Institute of Advanced Cross-field Science, College of Life Sciences, Qingdao University, Qingdao 200671, China
[b] School of Materials Science and Engineering, Jiulonghu Campus, Southeast University, Nanjing 211189, China
[c] China State Key Laboratory of Materials-Oriented Chemical Engineering, College of Chemical Engineering, Nanjing Tech University, Nanjing 210009, China

ARTICLE INFO

Article history:
Received 31 May 2022
Revised 5 July 2022
Accepted 17 August 2022
Available online 20 August 2022

Keywords:
Aqueous zinc-ion battery
Metal-organic frameworks
Cathode material
Excellent cycle performance
Zinc storage mechanism

ABSTRACT

Rechargeable aqueous zinc-ion batteries (AZIBs) are attracting tremendous attention because of their intrinsic merits such as high safety and low cost. Cathode plays a critical role in enhancing the electrochemical performance of AZIBs. However, it is difficult to design a robust and high-efficiency cathode material and further implement the commercialization of AZIBs. Metal-organic frameworks (MOFs) electroactive compounds are attractive to serve as the cathode of AZIBs due to their unique porosity and crystal structures, resource renewability and structural diversity. In this work, a calcium-pure terephthalates acid framework (Ca-PTA·3H_2O) was synthesized by facile hydrolysis and cationic exchange method, then explored as a novel cathode for AZIBs. The results highlight a high specific capacity of 431 mAh/g (0.51 mAh/cm^2) at a current density of 50 mA/g, and excellent cycle performance with capacity retention of ~90% after 2700 cycles at 500 mA/g. The following up characterizations investigate the reversible zinc storage mechanism in detail. This experiment made a specific contribution to the exploration of the new MOF as a competitive cathode for AZIBs.

In recent few decades, with the increasing prominence of non-renewable energy issues and promoting the realization of carbon neutrality, the search and utilization of clean energy resources are becoming the spotlight of worldwide research [1]. This has led to a fast growing demand for electrical energy, particularly in secondary batteries [2]. Lithium-ion batteries (LIBs) as a typical representative of secondary batteries with high energy density have been used as power sources in many fields. However, the limited resource of lithium and safety issues hindered its wide application [3,4]. Moreover, the evolution of sodium-ion batteries (SIBs) and potassium ion batteries (PIBs) was impeded by using volatile, flammable, and toxic organic electrolytes to some extent [5,6]. Based on these considerations, the interest in safe and resourceful aqueous rechargeable zinc-ion batteries (AZIBs) have re-emerged over the past years [7,8]. Besides, AZIBs possess advantages in their low redox potential and high ionic conductivity which is almost two orders of magnitude higher than those of non-aqueous electrolytes [9,10]. Nevertheless, the applications of AZIBs in energy storage field has bottlenecked by the insufficient energy density and limited life span. The dominating strategies for enhancing electrochemical performance involve the design of cathode materials [11], optimization of electrolytes [12], and modification of Zn anode [13,14]. In general, Zn^{2+} has higher electric charge and molecular weight, which makes ions more difficult to insert/extract into/from electrode materials [15]. Hence, the design and development of cathode material become the key aspect for the development of AZIBs.

The ZIB cathode materials developed so far range from Mn-oxides (MnO_2 with α-, β-, γ-, δ- and $ZnMn_2O_4$) [16–21], Prussian blue analogues [22], V-oxides (V_2O_5, VO_2, $Zn_{0.25}V_2O_5 \cdot nH_2O$, $H_2V_3O_8$, $NaCa_{0.6}V_6O_{16} \cdot 3H_2O$, V_6O_{15}) [23–26] to organic compounds (conductive polymer polyaniline, PANI, carbonyl compounds, polypyrrole, quinone) [27–29]. Yet, the long-term commercial use of most cathode materials is restricted by low-storage, poor rate performance, rapid capacity fading, toxicity, and limited inorganic mineral resource. It is urgent for AZIBs to discover new cathode materials with excellent electrochemical properties and renewability [30]. Benefit from the absolute superiority that C, H, O, N and S elements are abundant on the earth and the increased concerns about the environment, rechargeable batteries based on organic electrodes, such as lithium-ion batteries (LIBs) and sodium-ion batteries (SIBs), are burgeoning [31]. Indeed, many

* Corresponding authors.
E-mail addresses: fanqi1984@126.com (Q. Fan), yzhang_iacs@qdu.edu.cn (Y. Zhang).

https://doi.org/10.1016/j.cclet.2022.107760
1001-8417/

metal-organic frameworks (MOFs) have been explored as novel electrode materials for secondary energy storage devices, based on their properties of huge variety of structures, large surface areas and adjustable porosity. Such as, Armand and coworkers explored the performance of $Li_2C_8H_4O_4$ as the electrode of LIBs [32]. Xu's group has synthesized five kinds of MOFs materials, including Mn(BTC), Mn(BDC), Fe(BDC), Co(BDC), and V(BDC) (in which BDC is 1,4-dicarboxybenzene and BTC is 1,3,5-benzenetricarboxylic acid) and investigated their electrochemical behaviors as ZIB cathodes [33]. Nevertheless, some of these metal-organic electrodes are unstable in electrolytes, which may result in unstable electrochemical performance. Also, the reaction mechanism of those MOFs based energy storage devices is still elusive.

Purified terephthalic acid (PTA) is an optimized ligand used in the synthesis of MOFs due to its easy availability from cheap poly-ethylene terephthalate (PET) plastic products. Metal ions that possess higher ionization energy and larger ion radius coordinate with organic anions can increase the stability of electrodes in electrolytes [34]. In this work, a calcium-pure terephthalates acid metal-organic framework (Ca-PTA·$3H_2O$) is synthesized by facile hydrolysis and cationic exchange method and studied as an unexplored cathode for AZIBs. The Ca-PTA·$3H_2O$ cathodes delivered a high-specific capacity of 431 mAh/g (0.51 mAh/cm^2) at 50 mA/g, along with ~90% capacity retention (500 mA/g) after 2700 cycles. In addition, the storage mechanism of Zn^{2+} was studied by using *ex-situ* measurements. Results show that, on the one hand, Ca-PTA·$3H_2O$ can render a voltage plateau of ~1.45 V as well as the $CaSO_4{\cdot}2H_2O$ generated from extraction Ca^{2+} of Ca-PTA·$3H_2O$ facilitates the cycle stability, on the other hand, the generation of reversible discharging product $Zn_4SO_4(OH)_6{\cdot}4H_2O$ and intermediate compound $Zn_xMnO(OH)_y$ co-contributed to the high reversible capacity of the battery at activation stage.

The Ca-PTA·$3H_2O$ was synthesized as follows: briefly, 2 mmol NaOH (Aladdin, analytically pure) and 1 mmol Pure Terephthalic acid (H_2TP, Aladdin, 99%) were dissolved in 30 mL of de-ionized water in a beaker. The white suspension liquid was vigorously stirred for 10 h, after this, the solution became transparent. Then, 2 mmol $CaCl_2$ (Aladdin, analytically pure) was dissolved in 10 mL of de-ionized water and added into the above clear solution drop by drop. After about 10 min, the white precipitate appeared. Afterward, the beaker was covered with plastic wrap and heated to 80 °C in water bath, stirring constantly for 12 h to complete the exchange of Na^+ by Ca^{2+}. The precipitate was centrifuged and washed with de-ionized water several times. Finally, the product was dried at 60 °C overnight under vacuum.

The X-ray diffraction (XRD) pattern of Ca-PTA·$3H_2O$ was detected by a Rigaku II X-ray diffraction spectrometer (Japan Science Co., Tokyo, Japan) using Cu-Kα radiation ($\lambda = 0.15418$ nm). 2-theta degree was determined by range of 5° to 70°. Scanning electron microscopy (SEM) images were taken by a JEOL JSM-7800F microscope (Japan Electronics Co., Tokyo, Japan). Morphology of Ca-PTA·$3H_2O$ and its particles after circulation were measured by SEM and *ex-situ* SEM. X-ray photoelectron spectroscopy (XPS) was carried out on a Thermo Scientific ESCALab 250Xi+ X (Thermo Fisher Scientific Co., Waltham, America), the valence states were measured by XPS. Fourier transform-infrared (FT-IR) spectroscopy was performed using a Frontier NIR Std spectrophotometer (Thermo Fisher Scientific Co., Waltham, America). The thermal gravimetric analyses were conducted on Ltd STA409PC, DSC404F3 from the Setaram Instrumentation (France).

The CR2032 corn-type cells (Canrd Co., Guangdong, China) were used for AZIB electrochemical performance tests. The cell consisted of a Ca-PTA·$3H_2O$ cathode, a zinc anode with a diameter of 12 mm (Canrd Co., Guangdong, China), a glass fiber separator (diameter-16 mm Whatman Co., Maidstone, England) and 2 mol/L $ZnSO_4$ with 0.2 mol/L $MnSO_4$ aqueous electrolyte. A conventional slurry-coating process on titanium foils was used to fabricate the electrodes. The slurry was made of 70 wt% Ca-PTA·$3H_2O$ powder, 20 wt% acetylene black (AB) and 10 wt% polyvinylidene fluoride (PVDF, Macklin, $M_w = 1{,}000{,}000$) in an agate mortar. After slurry-coating, titanium foils were dried out at 60 °C for 12 h in a vacuum oven. The loading of Ca-PTA·$3H_2O$ electrode is about 1.8 mg/cm^2, corresponding to the active materials of around 1.3 mg/cm^2. Galvanostatic charge-discharge (GCD) was performed on a LAND battery test system CT3001A (Wuhan LAND Electronic Co., Ltd., Wuhan, China) in a voltage range of 0.8-1.85. Cyclic voltammetry (CV) measurements were carried out on a CHI760E electrochemical workstation (Shanghai Chenhua Instrument Co., Shanghai, China) at scan rate (0.3 mV/s).

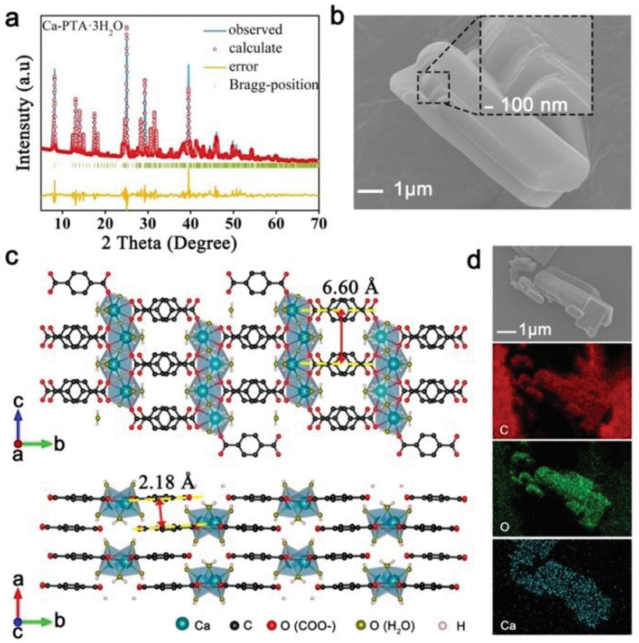

Fig. 1. (a) XRD refinement pattern of as-synthesized Ca-PTA·$3H_2O$. (c) Crystal structure of Ca-PTA·$3H_2O$. (b) SEM images and (d) EDS mapping of the synthesized Ca-PTA·$3H_2O$.

The Ca-PTA·$3H_2O$ was synthesized by facile hydrolysis and cationic exchange method. To identify the phase composition of the as-prepared samples, XRD measurements were performed and shown in Fig. 1a. Collected patterns display sharp peaks and are in line with the simulated patterns from the single crystal data (JCPDS No. 46-1873 $CaC_6H_4O_4{\cdot}3H_2O$, space group *P21/c*, lattice parameters $a = 7.11$Å, $b = 21.66$ Å, $c = 6.60$ Å, $\beta = 92.29°$), indicating the high crystallinity and purity of as-synthesized material [32]. Fig. 1c is a view of the crystalline framework of Ca-PTA·$3H_2O$ along *a* and *c* axis. Briefly, the Ca-carboxylate layer structure with 8-coordinated Ca^{2+} (four H_2O, four O each calcium ion) forms the dodecahedral. This layer structure is advantageous for the diffusion of Zn^{2+}. The molecular structure of CaTPA·$3H_2O$ powder and the properties of bonds are exhibited in Fig. S1 (Supporting information). The Ca^{2+} is connected to -COO(I) and shares the delocalized electrons of two oxygen atoms. The -COO(II) is coordinated with the H_2O molecules by hydrogen bonds. Fig. 1b displays the morphologies of as-synthesized Ca-TPA·$3H_2O$ which were investigated using scanning electron microscopy (SEM), this micro-particle with smooth surface is composed of layers. And the EDS mapping (Fig. 1d) demonstrates a well distribution of C, O and Ca elements of particles.

Fig. 2a shows the FT-IR spectrum of the as-prepared Ca-PTA·$3H_2O$. The broad bands with the peak at 3462 and 3280 cm^{-1}

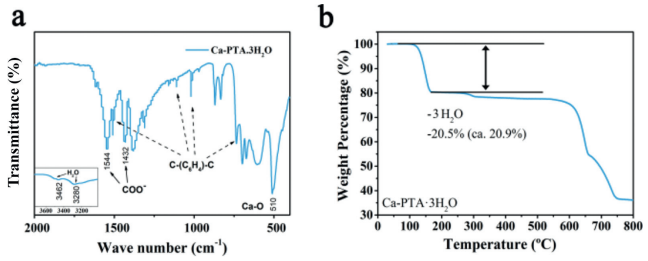

Fig. 2. (a) FTIR spectrum and (b) TGA curve of as-prepared Ca-PTA·3H_2O.

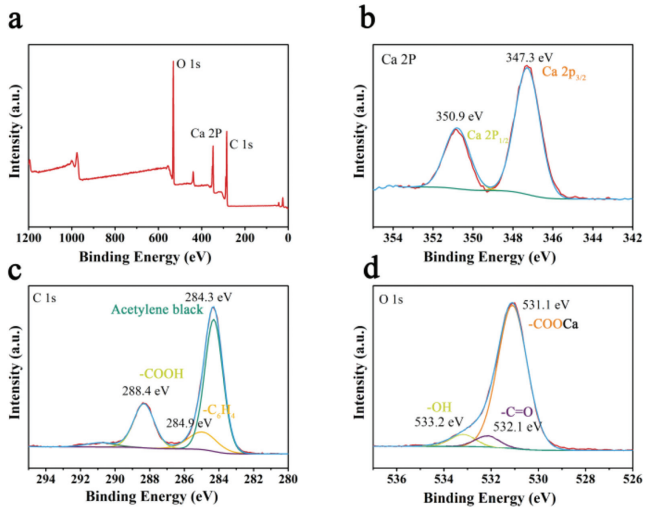

Fig. 3. (a) XPS survey spectra of the as-prepared Ca-PTA·3H_2O and narrow spectra for (b) Ca 2p (c) C 1s and (d) O 1s.

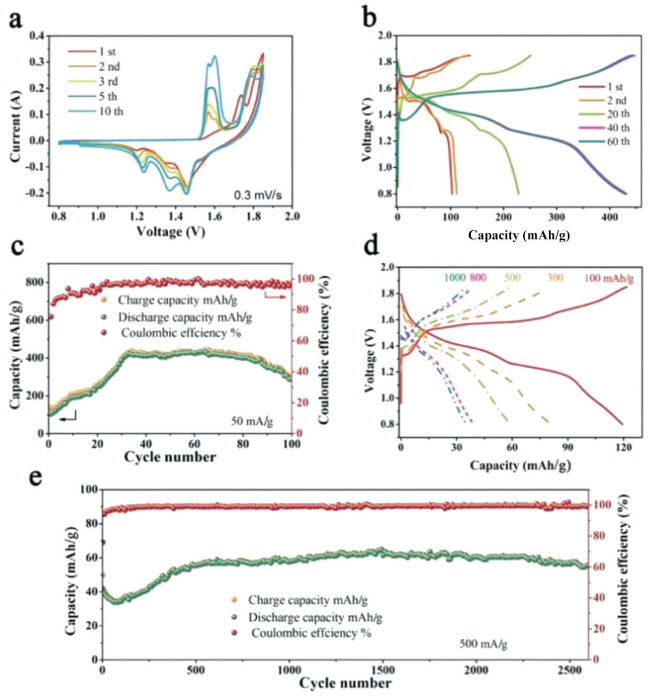

Fig. 4. (a) CV curves. (b) Voltage profiles. (c, e) Cycling performance. (d) Rate performance of Ca-PTA·3H_2O cathode.

are due to the coordinated H_2O. Compare to PTA ligands (Fig. S2 in Supporting information), the vanish of the typical C=O stretching vibration at 1674 cm^{-1} in addition to the δOH^- and νCO coupling vibration of carboxylic acid (-COOH) groups observed at 1286 and 924 cm^{-1} demonstrates a complete reaction in our synthesis procedure. After coordination with Ca^{2+}, there are two new bands located at 1544 and 1432 cm^{-1} attributed to asymmetric and symmetric stretching of carboxylic acid. The peak at 510 cm^{-1} is the bending vibration of δ(Ca-O). The above change of characteristic functional group clearly proves that coordination with Ca^{2+} occurs and results in the formation of Ca-PTA·3H_2O.

Thermogravimetric analysis (TGA) curve of as-prepared Ca-PTA·3H_2O (Fig. 2b) from room temperature to 800 °C in air shows the first weight change step with the mass loss (20.5%) from 100 °C to 150 °C. According to the chemical formula $CaC_6H_4O_4 \cdot 3H_2O$, this is due to the removal of three coordinated water and agrees well with the value (20.9%) calculated according to its chemical formula. The weight loss in the range of 600-750 °C is attributed to the further thermal decomposition of $CaC_6H_4O_4$ to the mixture of $Ca(OH)_2$, CaO and $CaCO_3$ (Fig. S3 in Supporting information). The TGA curve also indicates the successful synthesis of Ca-PTA·3H_2O.

To identify composition and valence state of Ca-PTA·3H_2O, X-ray photoelectron spectroscopy (XPS) was taken and presented in Fig. 3. The sharp peaks observed in the survey spectrum are O 1s, Ca 2p and C 1s, respectively (Fig. 3a). In Fig. 3b, two peaks existing at 347.3 and 350.9 eV displays doublets for Ca $2p_{3/2}$ and Ca $2p_{1/2}$ and spin-orbit splitting for the Ca $2p_{3/2}$ and Ca $2p_{1/2}$ is 3.6 eV. This is derived from the calcium atoms that are successfully bounded with a carboxyl group [35]. The emission peaks of the C 1s are displayed in Fig. 3c. The large peak at low energy is assigned to Acetylene black. The other two peaks centered at 284.9 and 288.4 eV are attributed to phenyl carbons (-C_6H_4) and carboxyl carbons (-COOH) [36,37]. Fig. 3d exhibits emission peaks of O 1s. In accordance with previous observations and the molecular structure of CaTPA·3H_2O in Fig. S1, the two contributions located at 532.1 eV and 533.2 eV are assigned to oxygen in the hydroxyl (C-OH) and carbonyl (C=O) groups of carboxyl(II) which is coordinated to the water molecules. The peak positioned at 531.1 eV is identified as two chemically identical oxygen in carboxyl(I) which is coordinated to calcium that Ca^{2+} shares the delocalized electrons from two O atoms [38]. Consequently, this layered structured composites Ca-PTA·3H_2O was successfully synthesized.

The electrochemical performance of Ca-PTA·3H_2O as the cathode of AZIBs with a voltage window between 0.80-1.85 V is explored. Using classic $ZnSO_4$ (2 mol/L)+$MnSO_4$ (0.2 mol/L) as electrolyte, the cyclic voltammetry (CV) curves at a scan rate of 0.3 mV/s and the galvanostatic charge and discharge (GCD) profiles at 50 mA/g were displayed in Figs. 4a and b, respectively. The curve of the first charge process is different from the following cycles, so we studied the phase change of the battery's first charge process. From *ex-situ* XRD pattern (Fig. S4 in Supporting information) we can see the emergence of $CaSO_4 \cdot 2H_2O$, which indicates that some extracted Ca^{2+} of Ca-PTA·3H_2O diffuse into to the electrolyte and form insoluble $CaSO_4 \cdot 2H_2O$ on the electrode surface. Therefore, those oxidation peaks can be mainly ascribed to the extraction of Ca^{2+} and phase change process of cathode material. The reduction peaks in the first discharge process are attributed to the zinc ion multi-insertion [39]. After the first cycle, the wide oxidation peaks at ~1.57 V and the corresponding reduction peaks at around 1.30 V are attributed to sedimentation/resolution of manganese and $Zn_4SO_4(OH)_6 \cdot 4H_2O$ on electrode surface. It also could be observed that those new redox peaks have a mildly rising in the following cycles which is consistent with the rising specific capacity observed in Figs. 4c and e. According to some recent studies [40], the assisted deposition-dissolution of $Zn_4SO_4(OH)_6 \cdot 4H_2O$ can co-contribute to a high capacity, which is common in Mn^{2+}-containing AZIB systems. The mildly rising peak intensity is meant for the gradual battery activation. Another pair of redox peaks suited at ~1.8 V/~1.45 V remain stable. This strong and stable

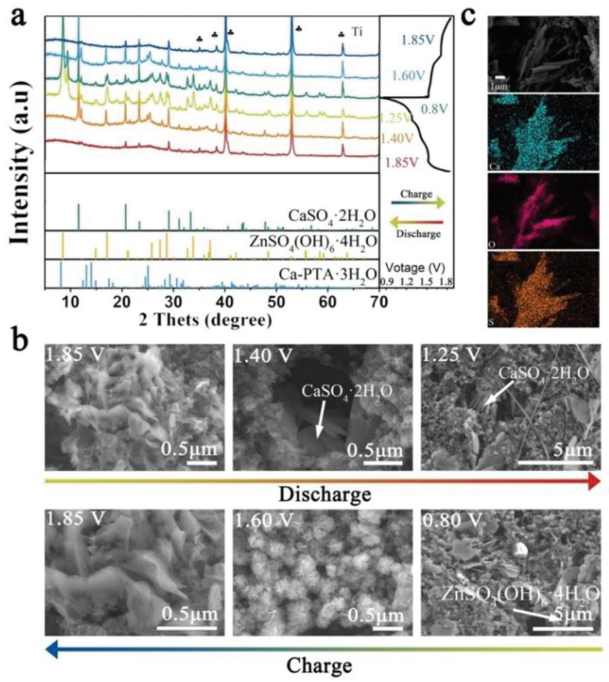

Fig. 5. (a) *Ex-situ* XRD patterns and (b) *ex-situ* SEM images of the Ca-PTA·$3H_2O$ cathode taken at different stages during a charge-discharge cycle of battery activation stage. (c) The EDS mapping of "rod-like" $CaSO_4·2H_2O$ particles.

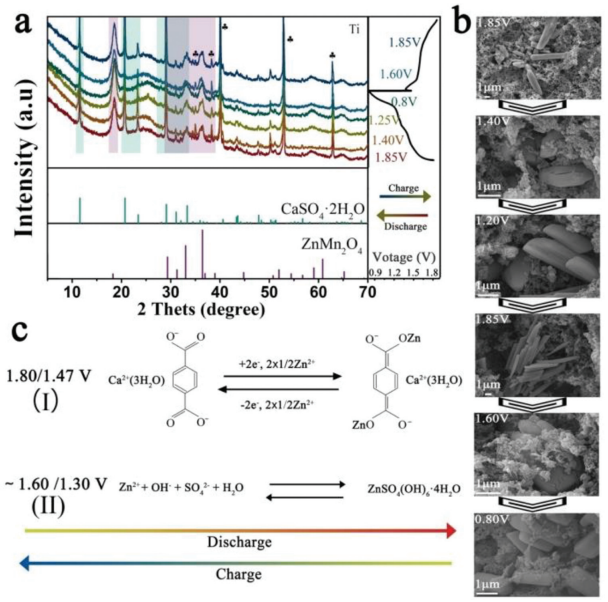

Fig. 6. (a) *Ex-situ* XRD patterns and (b) *ex-situ* SEM images of the Ca-PTA·$3H_2O$ cathode taken at different stages during a charge-discharge cycle of battery stable stage. (c) Schematic illustration of the Zn^{2+} insertion/extraction at different discharge/charge platforms.

couple of redox peaks mainly derives from the reversible insertion/extraction of Zn^{2+} into/from Ca-PTA·$3H_2O$. In keeping with the CV curves, a repeatable discharge voltage plateau at about 1.45 V could be observed in the voltage profiles (Fig. 4b). After the activation process, the specific capacity stabilizes at 431 mAh/g (0.51 mAh/cm^2 at 50 mA/g). Fig. 4d show the discharge-charge curves at different current density. The reversible capacity summarized as 121, 80, 59, 39, 35 mAh/g, at 100, 300, 500, 800, 1000 mA/g, respectively. All the pseudo-plateau at larger current density matched those at 50 mA/g. And the prolonged cycle performance testing at 500 mA/g is shown in Fig. 4e. After 2700 cycles, the specific capacity retention is ~90%. Both the GCD curves at low (Fig. 4c) and high (Fig. 4e) current density are highlighting the excellent cycle stability. In addition, Table S1 (Supporting information) compares the electrochemical performances of many reported cathode materials used in AZIBs with that of Ca-PTA·$3H_2O$, clearly indicating its competitive performance.

To analyze the Zn^{2+} storage mechanism of Ca-PTA·$3H_2O$, some detailed characterizations were performed. The data of *ex-situ* XRD, *ex-situ* XPS and *ex-situ* SEM are recorded to probe the reversible changes of cathode.

The phase and morphology evolution of the Ca-PTA·$3H_2O$ cathode during a GCD cycle of battery activation stage is shown in Fig. 5. The *ex-situ* XRD and SEM patterns of the cathode are taken at different states (1.85, 1.40, 1.25, 0.80, 1.60 and 1.85 V). The prominent peaks of MOF-73 disappear, indicating that the structure of Ca-PTA·$3H_2O$ gradually converted along with each charge and discharge process. The peak intensity that in/decreases during the discharge/charge process from 1.85 V to 1.40 V/1.60 V to 1.85 V belongs to $CaSO_4·2H_2O$, corresponding to the insertion/extraction of Zn^{2+} into/from cathode material and the formation of $CaSO_4·2H_2O$. The "rod-like" particles are shown in the surface morphology evolution of the electrode at 1.4 and 1.25 V in Fig. 5b. Also, EDS mapping (Fig. 5c) shows that the Ca, O and S elements are uniformly distributed in the "rod-like" particles. Unifies the *ex-situ* XRD date, this "rod-like" particle is $CaSO_4·2H_2O$. Ca^{2+} species extract from Ca-PTA·$3H_2O$ and form insoluble $CaSO_4·2H_2O$ which facilitates the stability of electrochemical performance [39]. The emergence (from 1.4 V to 0.8 V) and vanishment (from 0.8 V to 1.6 V) of $Zn_4SO_4(OH)_6·4H_2O$ characteristic peaks also can be observed in the patterns. It is because the insertion/extraction of partial Zn^{2+} and H^+ was accompanied by the deposition-dissolution of the $Zn_4SO_4(OH)_6·4H_2O$ [41]. As a consequence, the $Zn_4SO_4(OH)_6·4H_2O$ nanoplates can be observed at the voltage states of 1.25 and 0.80 V (Fig. 5b). When discharged to 1.40 V and charge to 1.60 V, many "nanoflower-like" particles appear, which we assumed as intermediate compound $Zn_xMnO(OH)_y$. The EDS mapping (Fig. S5a in Supporting information) shows that these particles contain O, Zn and Mn elements and absence of S elements that also matches well with previous reports [42,43].

To further investigate the Zn^{2+} storage mechanism during the charge-discharge process at battery stable stage, the *ex-situ* XRD and SEM are characterized and displayed in Figs. 6a and b. Different from the reversible phase change at battery activation stage, the *ex-situ* XRD patterns of battery stable stage remain constant during the GCD cycle. Particularly, the peaks can fit well with $CaSO_4·2H_2O$ and $ZnMn_2O_4$. The $CaSO_4·2H_2O$ is derived from the extracted Ca^{2+} from Ca-PTA·$3H_2O$ and embedded in the electrode. This result is verified by the *ex-situ* SEM (Fig. 6b). The $ZnMn_2O_4$ is a byproduct generated from Mn^{2+}-contained electrolyte proceed along the electrochemical reaction displayed in Eq. S1 (Supporting information) [44].

Based on the above discussion, a proposed conversion Zn^{2+} storage mechanism at battery activation stage of Ca-PTA·$3H_2O$ cathode is illustrated in Fig. 6c. (I) and (II) electrochemical redox paths correspond to their platforms in the GCD curves, respectively. When battery goes to stable stage, there is no phase evolution but Zn^{2+} insertion/extraction. According to the electrochemical mechanism of this kind of MOF electrode material in LIBs and SIBs, the reaction of Ca-PTA·$3H_2O$ is a two-electron transfer reaction and offers a theoretical capacity of 207.57 mAh/g relying on the reversible reaction of two –C=O groups. Meanwhile, We observe that the practical capacity, especially at low current densities, is higher than the theoretical capacity, which proba-

bly comes from the sedimentation/resolution of manganese and $Zn_4SO_4(OH)_6{\cdot}4H_2O$ on the electrode surface.

In summary, we have fabricated an ultra-stable aqueous Zinc-ion batteries system using an unexplored AZIBs cathode material Ca-PTA·$3H_2O$. As a result, a high specific capacity of 431 mAh/g (0.51 mAh/cm^2) and outstanding cycling stability is achieved by the co-contribution of Zn^{2+} insertion/extraction into/from Ca-PTA·$3H_2O$ and sedimentation/resolution of manganese and $Zn_4SO_4(OH)_6{\cdot}4H_2O$ on the electrode surface. The *ex-situ* measurements reveal that after the activation stage, Ca^{2+} species extract from Ca-PTA·$3H_2O$ and form insoluble $CaSO_4{\cdot}2H_2O$ which facilitates the stability of electrochemical performance (after 2700 cycles, the specific capacity retention is ∼90% at 500 mA/g). The unchanged phase and morphology deliver the stable electrochemical behaviors of cathode material. This work provides a new way for the development of high-performance aqueous Zinc-ion batteries based on the MOFs.

Declaration of competing interest

The authors declare that they have no known competing financial interests or personal relationships that could have appeared to influence the work reported in this paper.

Acknowledgments

This work was supported by the discipline construction funds from Qingdao Municipal Science and Technology Commission and Qingdao University (Nos. DC1900013623 and DC2000003363) as well as by Youth Project of Natural Science Foundation of Shandong Provincial (No. ZR2021QB175). This work is also supported by Natural Science Foundation of Shandong and National Natural Science Foundation of China (No. 51877045), the Foundation from State Key Laboratory of Materials Oriented Chemical Engineering (No. KL19-09) the Fundamental Research Funds for the Central Universities.

Supplementary materials

Supplementary material associated with this article can be found, in the online version, at doi:10.1016/j.cclet.2022.107760.

References

[1] S. Chu, Y. Cui, N. Liu, Nat. Mater. 16 (2017) 16–22.
[2] D.Z. Chao, W.H. Xie, F.X. Ye, et al., Sci. Adv. 6 (2020) eaba4098.
[3] B. Dunn, H. Kamath, J.M. Tarascon, Science 334 (2011) 928–935.
[4] T. Jiang, S.Y. Ma, J.B. Deng, et al., Adv. Sci. (2021) 2105119.
[5] D. Chao, B. Ouyang, P. Liang, et al., Adv. Mater. 30 (2018) 1804833.
[6] W. Zhang, Y. Liu, Z. Guo, Sci. Adv. 5 (2019) eaav7412.
[7] Y. Gao, H. Yang, Y. Bai, et al., J. Mater. Chem. A 9 (2021) 11472–11500.
[8] C. Xie, Q. Zhang, Z. Yang, et al., Chin. Chem. Lett. 33 (2022) 2653–2657.
[9] D. Kundu, S.H. Vajargah, L.W. Wan, et al., Energy Environ. Sci. 11 (2018) 881–892.
[10] X.H. Zeng, J.N. Hao, Z.J. Wang, et al., Energy Stor. Mater. 20 (2019) 410–437.
[11] M. Song, H. Tan, D.L. Chao, et al., Adv. Funct. Mater. 28 (2018) 1802564.
[12] F. Wan, J. Zhu, S. Huang, et al., Batter. Super. 3 (2020) 323–330.
[13] Z. Guo, L. Fan, C. Zhao, et al., Adv. Mater. 34 (2022) e2105133.
[14] Y. Zhang, X. Li, L. Fan, et al., Cell Rep. Phys. Sci. 3 (2022) 100824.
[15] L.S. Ma, M.A. Pollard, T.P. Borodin, et al., Energy Environ. Mater. 3 (2020) 516–521.
[16] M.H.M. Alfaruqi, V. Gim, J. Kim, et al., Chem. Mater. 27 (2015) 3609–3620.
[17] C.L. Guo, H.M. Li, J.F. Hou, et al., Electrochim. Acta 304 (2019) 370–377.
[18] H.L.S. Pan, Y.Y. Yan, et al., Nat. Energy 1 (2016) 16039.
[19] M.J.W. Shi, B. Shen, Y. Jiang, et al., Chem. Eng. J. 399 (2020) 125627.
[20] M.L. Sun, D.S. Wang, Y.F. Liu, et al., ChemElectroChem 6 (2019) 2510–2516.
[21] N.C. Zhang, F.Y. Liu, J.X. Wang, et al., Nat. Commun. 8 (2017) 405.
[22] L.Y. Zhang, L. Chen, X.F. Zhou, et al., Adv. Energy Mater. 5 (2015) 1400930.
[23] P. He, M.Y. Yan, G.B. Zhang, et al., Adv. Energy Mater. 7 (2017) 1601920.
[24] Z.L. Li, S. Ganapathy, et al., Adv. Energy Mater. 9 (2019) 1900237.
[25] H.G. Qin, L.L. Chen, L.M. Wang, et al., Electrochim. Acta 306 (2019) 307–316.
[26] N. Zhang, M. Jia, Y. Dong, et al., Adv. Funct. Mater. 29 (2019) 1807331.
[27] Z. Chen, T.M. Liu, Z.M. Zhao, et al., J. Power Sources 457 (2020) 227994.
[28] H. Jia, Z.Q. Wang, B. Tawiah, et al., Nano Energy 70 (2020) 104523.
[29] X.Y. Liu, J. Wu, K. Jiang, et al., Nanotechnology 31 (2020) 122001.
[30] L.W. Guo, K.M. Liu, B. Wang, et al., Nanotechnology 32 (2021) 442001.
[31] T.F. Liu, C.J. Tong, B. Wang, et al., Adv. Energy Mater. 9 (2019) 1803390.
[32] L. Wang, C. Mou, Y. Sun, et al., Electrochim. Acta 173 (2015) 235–241.
[33] X.J. Pu, B. Wang, X. Liu, et al., Nanomicro Lett. 12 (2020) 152.
[34] Y. Zhang, Y. Niu, M.Q. Wang, et al., Chem. Commun. 52 (2016) 9969–9971.
[35] B. Demri, D. Muster, J. Mater, Process. Tech. 55 (1995) 311–314.
[36] M.Q. Wang, C. Ye, S.J. Bao, et al., Analyst 141 (2016) 1279–1285.
[37] W.H. Zhang, A. Nefedov, M. Naboka, et al., Phys. Chem. Chem. Phys. 14 (2012) 10125–10131.
[38] S. Stepanow, T. Strunskus, M. Lingenfelder, et al., J. Phys. Chem. B 108 (2004) 19392–19397.
[39] S. Guo, S. Liang, B. Zhang, et al., ACS Nano 13 (2019) 13456–13464.
[40] H. Chen, S. Cai, Y. Wu, et al., Mater. Today Energy 20 (2021) 100646.
[41] X.W. Shen, X.N. Zhou, Y.R. Shi, et al., Adv. Funct. Mater. 31 (2021) 2101579.
[42] Y.F. Huang, J. Mou, W.B. Liu, et al., Nano-Micro Lett. 11 (2019) 49.
[43] T.S. Zhang, Y. Tang, G.Z. Feng, et al., Adv. Funct. Mater. 30 (2020) 2002711.
[44] H. Yang, W. Zhou, D. Chen, et al., Energy Environ. Sci. (2022) 1106–1118.